Analytica Chimica Acta 1007 (2018) 26–32

Contents lists available at ScienceDirect

Analytica Chimica Acta

journal homepage: www.elsevier.com/locate/aca

Single cell patterning for high throughput sub-cellular toxicity assay

Junfei Xia [a], Yuting Qiu [a], Xiaojie Xun [a], Liyuan Ma [a], Jingjiao Guan [b], Ming Su [a, *]

[a] Department of Chemical Engineering, Northeastern University, Boston, MA 02115, USA
[b] Department of Chemical and Biomedical Engineering, Florida State University, Tallahassee, FL 32310, USA

HIGHLIGHTS

- Single cell array is made by selective cell adhesion onto lithographically patterned surface.
- Population based toxicity, single cell toxicity, and subcellular toxicity are derived simultaneously at high throughput.
- Issues of cell overlapping and clustering are completely solved.
- Imaging software allowed for rapid, objective and automated extraction of toxicity information without user interference.

GRAPHICAL ABSTRACT

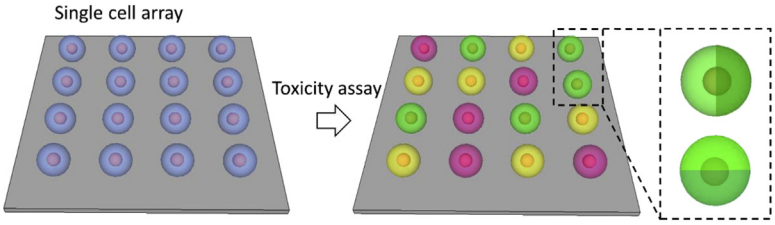

ARTICLE INFO

Article history:
Received 28 July 2017
Received in revised form
16 November 2017
Accepted 17 November 2017
Available online 23 November 2017

Keywords:
Single cell patterning
Cell population
Sub-cellular heterogeneity
Radiation
Toxicity

ABSTRACT

Cell population based toxicity assays cannot distinguish responses of single cells and sub-cellular organelles; while single cell assays are limited by low statistical power due to small number of cells examined. This article reports a new single cell array based toxicity assay, in which cell responses at population level, single cell level and sub-cellular level can be obtained simultaneously at high throughput. The single cell array was produced by microcontact printing and selected area cell attachment, and exposed to damaging X-ray radiation, which was followed by fluorescence imaging after staining. Two image processing softwares written in Python and MATLAB were used to determine the expressions of proteins associated with cell migration and invasion, and production of reactive oxygen species (ROS), respectively. The results showed significant differences in responses at single cell level and distinctive molecular heterogeneity at sub-cellular level in a large population of cells upon exposure to radiation.

1. Introduction

A panel of in vitro toxicity assays has been developed to assess the effects of chemicals and external stimuli on cultured mammalian cells for drug screening and hazard identification [1–4]. The toxicity assays depend on cell functions such as enzyme activity, membrane permeability, adherence, adenosine triphosphate (ATP) and co-enzyme productions, and nucleotide uptake activity [5–7]. The assays can provide averaged signals from a large population of cells. However, due to cellular heterogeneity, the toxicity results derived from cell population can be irrelevant or misleading especially in the case of cancer which is known for high level of heterogeneity [8,9]. Furthermore, toxicity assays relying on non-image based readouts cannot reveal sub-cellular distribution of events and cannot help to understand the mechanism of responses. Fluorescence imaging allows mapping of spatial

* Corresponding author.
E-mail address: m.su@northeastern.edu (M. Su).

https://doi.org/10.1016/j.aca.2017.11.044
0003-2670/

distribution of cellular events with specific dyes, but is limited by cell overlapping issue and a small number of cells that can be counted under a microscope.

Single cell toxicity assay can distinguish the function and behavior of individual cells from a background of million cells, and identify subpopulations in a heterogeneous mixture of cells or cell sub-types [10–12]. Single cell toxicity assays are often performed in dynamic mode with flow cytometry or microfluidics, which has high linear speed, but does not provide information on cell-cell communication, cell morphology and sub-cellular features [13–17]. An ideal single cell toxicity assay should be able to provide cell information on three different levels: cell population, individual cells, and sub-cellular level, which are required for proper extrapolation of in vitro toxicity response to in vivo response [18,19]. In this perspective, an ordered array of cells attached on a planar substrate is a better choice by allowing observation of cell population, individual cells, and sub-cellular organelles [20–25]. Single cell array as a platform technology has been used for many biology-driven applications such as single cell fluorescence in situ hybridyzation (FISH), genotoxicity study, and RNA sequencing [26–28]. A variety of methods can be used to generate single cell arrays on a solid substrate after modifying the substrate with positively charged molecules, cell adhesive ligands, and specific antibodies [26,29–32]. By attaching cells onto the substrate, it is also feasible to conduct time-dependent analysis of cell population [23].

This article describes a single cell array based toxicity assay, in which population based toxicity, single cell toxicity, and sub-cellular toxicity can be derived simultaneously and at high throughput (Fig. 1). The single cell array is made by attracting onto micropatches produced with microcontact printing of polyelectrolyte multilayers. Cell responses to ionizing radiation were simultaneously obtained at three distinct levels. By physically attaching cells at the same height and ordered locations, the issues of cell overlapping and clustering associated with random distribution were solved completely, and there is no need for a user to change observation field to find cells that can provide useful information. The image processing softwares developed in this work allowed rapid, objective and automate extraction of toxicity information without user interference. By uniquely providing population based assay with sub-cellular spatial resolution and single cell sensitivity, this method has the potential to significantly impact the toxicity field.

2. Materials and methods

Poly(allylamine hydrochloride) (PAH) with molecular weight of 120,000–200,000 was from Alfa Aesar. Poly(sodium 4-styrene sulfonate) (PSS) with molecular weight of 70,000, fluorescein isothiocyanate isomer I (FITC), monoclonal anti-vinculin-FITC antibody, and anti-β-tubulin antibody were from Sigma. Hydroxy(polyethyleneoxy) propyl triethoxysilane (PEG-silane) (8–12 ethylene oxide, 50% in ethanol) was from Gelest. Polydimethylsiloxane (PDMS Sylgard 184) was from Dow Corning. Goat anti-mouse IgG secondary antibody conjugated with Alexa Fluro 568, Hoechst 33342, and Carboxy-H2DCFDA were from ThermoFisher. Polyelectrolyte stock solutions were 1 wt% PAH at pH 10, 1 wt% PSS at pH 5.8, and 1% PAH at pH 5.8, all contain 150 mM NaCl.

A mixture of PDMS prepolymer and curing agent (10:1 wt ratio) was poured onto a master prepared by photolithography. After being kept at 37 °C for 24 h, the solidified PDMS slab was peeled off and cut into square stamps that have vertical micro-pillars with a diameter of 10 μm, a height of 5 μm, and a center-to-center distance of 30 μm in the hexagonal lattice. A glass slide was treated with high level oxygen plasma for 3 min, and soaked in PEG-silane solution (5% in ethanol) for overnight, and rinsed with water and dried with an air stream.

Single cell array is formed as follows. A 1 × 1 cm^2 PDMS stamp with micropillars was immersed in positive and negative polyelectrolyte solutions repeadly for 15 min each and rinsed with water to form multilayers. After drying in air, the stamp was exposed to vapor from a water bath, and immediately brought into contact with a PEG-coated slide for 20 min to allow water between stamp and slide to evaporate, which is followed by peeling off the stamp to complete the pattern transfer. To enclose cell suspension onto the patterned substrate, a PDMS slab with a 5 mm diameter hole was placed on the pattern to form a chamber, into which 200 μL cell suspension (5 × 10^5 cell/mL) in culture medium was added. The cells in chamber were incubated at 37 °C and 5% CO_2 for 1 h, followed by removing PDMS slab and washing the cell adhesion area gently with phosphate buffer saline (PBS) to remove unbound cells. The cells were immersed in PBS during the assay process.

CEM cells were cultured in RPMI 1640 medium supplemented with 10% (volume) fetal bovine serum (FBS), 100 units/mL of penicillin, and 100 μg/mL streptomycin at 37 °C and 5% CO_2. HeLa cells were cultured in DMEM medium supplemented with 10% fetal bovine serum (FBS), 100 units/mL of penicillin at 37 °C and 5% CO_2.

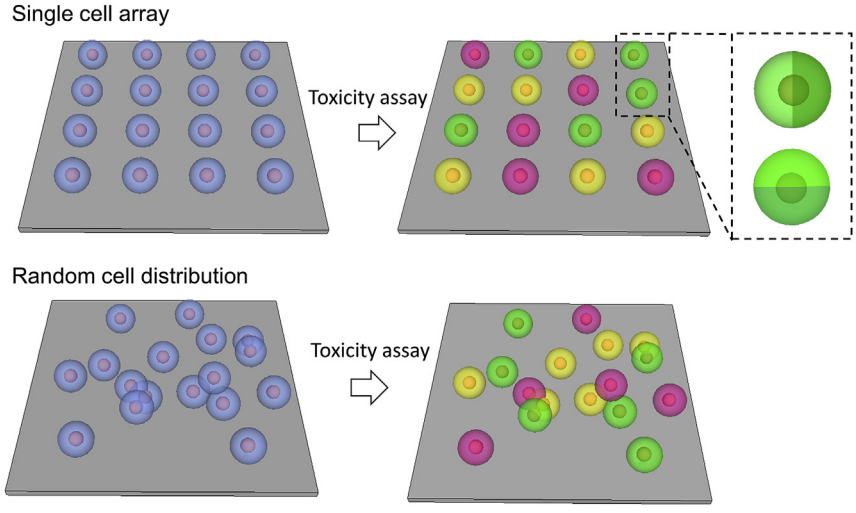

Fig. 1. Single cell patterning for high throughput sub-cellular toxicity assay.

Arrayed cells were irradiated with X-ray at 20 GY dose followed by 30 min incubation, and fixed in 4% paraformaldehyde for 10 min. After washing with 0.2% Triton-X 100 in PBS, cells were incubated in PBS with 0.2% Triton-X 100, and 1% bovine serum albumin (BSA) at room temperature. Primary antibody was added and incubated in blocking buffer at 4 °C overnight, followed by adding secondary antibody and incubated for 2 h. For ROS detection, carboxy-H_2DCFDA was added to arrayed cells at a final concentration of 20 μM. After incubation for 30 min and washed with PBS, cells were irradiated with X-ray at 20 GY dosage followed by 30 min incubation. Cell nuclei were stained with Hoechst 33342 at final concentration of 10 μM and fixed in 4% paraformaldehyde. All fluorescence images were obtained from an upright BX51 Olympus microscope and processed in Python and MATLAB.

3. Results and discussion

PAH is positively charged at neutral pH and can be adhesive to cells since many types of mammalian cells are negatively charged due to existence of sialic acid on their surfaces [33]. A wide variety of cell adhesion molecules such as arginylglycylaspartic acid (RGD), immunoglobulin G (IgG) and oleyl chain grafted to polyethylene glycol (PEG) can be applied to fabricate microarray, electrostatic interaction is used because of simplicity and low cost [34,35]. However it doesn't rule out the possibility that specific cell type can be patterned by specific interactions. PEG-coated surface is well known for its anti-fouling property and can prevent adhesion of cells [36]. Fig. 2A shows an array of multilayers composed of PAH/PSS/PAH-FITC printed on a PEG-coated glass slide, where PAH-FITC is PAH labelled with fluorescein isothiocyanate (FITC). Fig. 2B and C are microscopic images of arrays of CEM cells and Hela cells. The size of each micropatch is 10 μm, and the center-to-center distance is 30 μm, thus each patch can capture one cell without bridging two adjacent patches. The lack of bridging cells could be due to mobility of cells across non-patterned regions. Fig. 2D–F shows time-laps images of HeLa cells, where the white arrow pointed one cell moved towards the center of a green patch at the speed of 0.56 μm/min. This behavior has been observed in multiple cells ($n > 10$) and for adherent cells only probably due to higher motility compared to suspension cells. Since the directions of movement were random, the movement should not be caused by microscopic flow. The local movement facilitates formation of cell array and allows to use a small number of cells to obtain high array occupancy.

Radiation can cause damage to cells and tissues. At cellular level, radiation induces direct damage by breaking chemical bonds or indirect damage by producing reactive oxygen species which further attack nucleic acids, proteins and lipids. Arrayed HeLa cells were exposed to ionizing X-ray radiation from a generator operated at 115 kV and 5 mA. The impacts of radiation on genomic integrity, protein expression as well as ROS production were quantitatively analyzed. Fig. 3A and B shows Hoechst staining of DNAs in arrayed cells before and after radiation. Each nucleus in 3B is larger than that in 3A, indicating diffusion of DNA fragments outwards through broken nuclei membrane. This is different from HaloChip assay reported before [29], because damaged DNA cannot pass through cell membranes after fixation. The spatial distribution of the nuclear fluorescence can be used to quantify level of DNA damage. Fig. 3C shows a plot of fluorescence intensities along the red and green lines passing through centers of five adjacent cell nuclei. Fluorescence peaks of radiated sample are broader due to DNA leakage. The bandwidth of the peak can be quantified by full width at half maximum (FWHM). The FWHMs of five selected nuclei were obtained by fitting the curves using Gaussian distribution and calculated using the following formula in OriginLab,

$$FWHM = 2\sqrt{2ln2}\sigma$$

where σ stands for standard deviation. Fig. 3D shows statistical comparison between control and irradiated samples. The FWHM of cells are significantly larger after irradiation, suggesting increased DNA damage in these cells.

Ionizing X-ray irradiation can inhibit polymerization and aggregation of microtubules and induce disorganization of cytoskeletal filaments [37–40]. The change of protein expression was evaluated by immunostaining two types of cellular proteins associated with cell motility, where vinculin is a membrane-

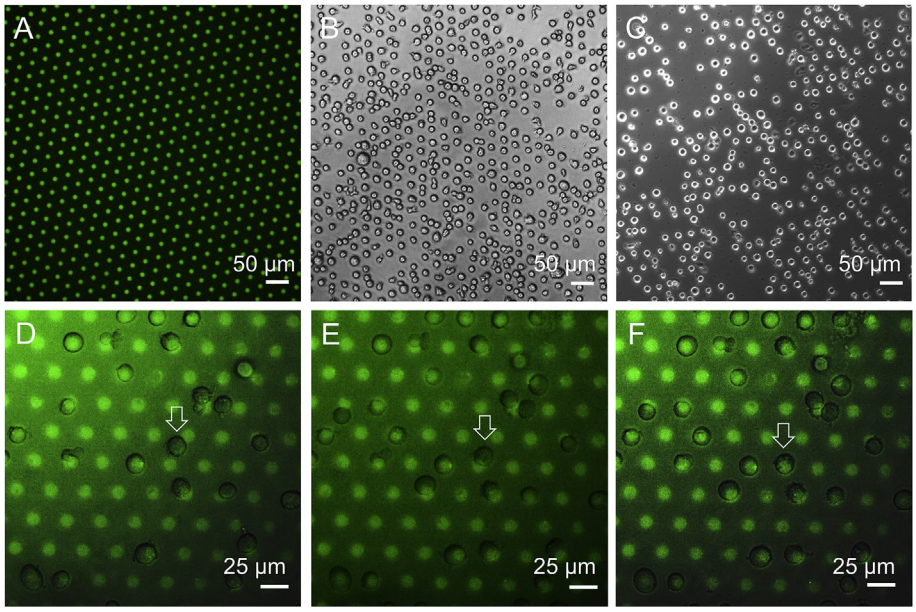

Fig. 2. An array of PAH/PSS/PAH-FITC on PEG (A). Single CEM cell array (B) and single HeLa cell array (C). Time-laps images of HeLa cell movement on the array at 0 min (D), 12 min (E) and 32.5 min (F).

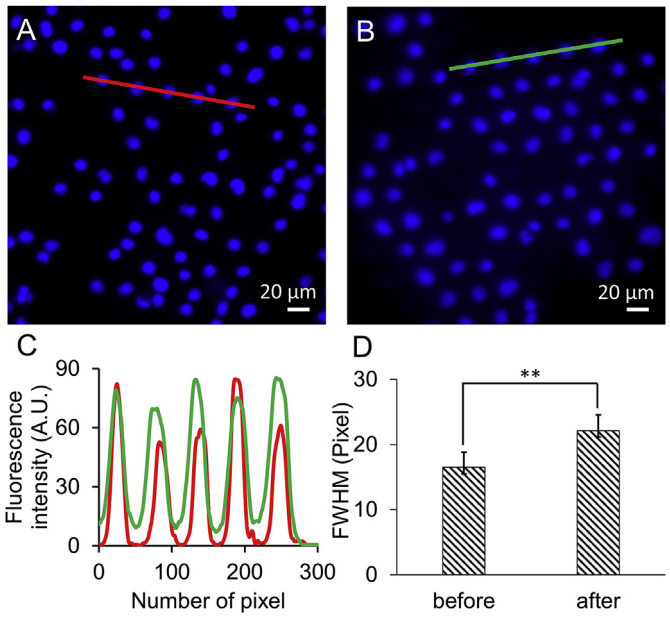

Fig. 3. Hoechst stained HeLa cells before (A) and after (B) X-ray radiation. (C) Fluorescence intensities of cells crossed by the lines in (A and B), where red line is from un-radiated sample and green line is from radiated sample. (D) Average FWHM of 41 cells before (A) and after (B) radiation. (For interpretation of the references to colour in this figure legend, the reader is referred to the web version of this article.)

cytoskeletal protein involved in focal adhesion and β-tubulin is a major component of microtubules. Both Fig. 4A and D shows extensive cytoskeletal networks from healthy cells, where green and red fluorescence were immunostaining of vinculin and β-tubulin. In radiated samples (Fig. 4B and E), fluorescence intensities were much lower and punctate structures were formed in some cells due to disassembly of cytoskeletal network. Radiation induced oxidative stress can also damage cells and cellular organelles, therefore can be assessed on a single cell array. Fig. 4G shows that non-irradiated cells contain negligible ROS signal (base level of cells), while cells exposed to radiation show strong ROS signal (Fig. 4H). Generation of ROS is highly time dependent in cells ranging from nanoseconds to a few days and the single cell array also provides ability for individual cell tracking [41].

By placing cells on an ordered array, cell images can be easily processed with softwares. Two sets of algorithms have been developed for Python and MATLAB to quantify fluorescence intensity of individual cells. The first algorithm (in Python) was based on segmenting the image into areas with identical sizes and with one cell per area. The information of each area was then extracted and analyzed. Mean intensity of each pixel in the area was calculated as intensity of the cell in that area. The second algorithm (in MATLAB) was based on setting an intensity threshold and grouping connected pixels with values above the threshold into isolated regions. Background noise was removed by deleting regions with size below that of a normal cell. The information of each region recognized as single cell, was then extracted, indexed and stored. The second algorithm was suitable for sub-cellular analysis since it already separated cellular information from background.

Fig. 4C shows histograms of fluorescence intensity of vinculin in the cell population before and after radiation, which were obtained after image processing. Black columns represent samples treated with 20 GY X-ray and red ones represent un-treated samples. Similarly, Fig. 4F shows histogram of fluorescence intensity of β-tubulin expression, where black column represents irradiated

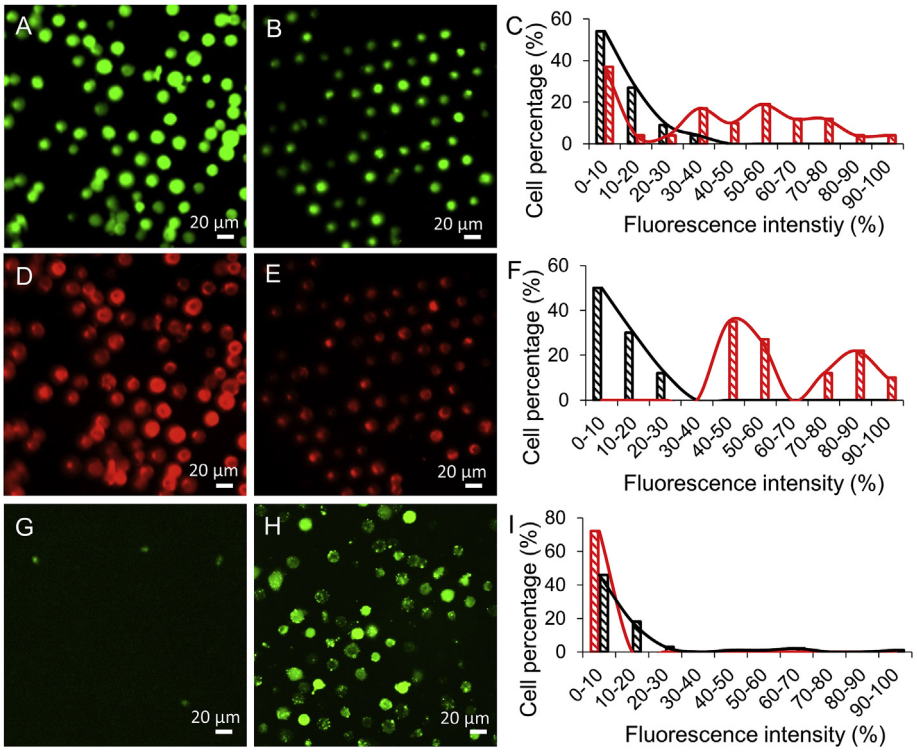

Fig. 4. Arrayed cells stained by anti-vinculin antibody before (A) and after (B) X-ray radiation. Arrayed cells stained by anti-β-tubulin antibody before (D) and after (E) X-ray radiation. Arrayed cells stained by H_2DCFDA before (G) and after (H) X-ray radiation. Histograms of fluorescence intensity in according figures (C is for image A and B; F is for image D and E; and I is for image G and H), where red bars stand for un-radiated samples and black bars stand for radiated samples. (For interpretation of the references to colour in this figure legend, the reader is referred to the web version of this article.)

samples and red ones represent un-treated samples. Shape of the histogram reveals existence of cell sub-populations. The total fluorescence intensities of vinculin and β-tubulin in un-treated sample are 5.6 and 5.3 times of those in irradiated samples, respectively. Fig. 4I shows histogram of fluorescence intensity of ROS production, where black columns stand for un-treated samples and red ones for radiated samples. The fluorescence intensity of radiated sample is much higher than un-treated one due to higher level of ROS production.

A major advantage of single cell array is that it allows for sub-cellular analysis of a large population of cells. MATLAB was used to quantify fluorescence intensity and distribution in individual cells. Fig. 5A shows ROS distribution inside single cell after radiation, where cell nuclei was stained with Hoechst, and green fluorescence indicated ROS signal. Distribution of green fluorescence was highly heterogeneous inside each cell (Fig. 5A inset) and had little overlap with the nucleus. Fig. 5B shows the image of a cell array processed by MATLAB in which region of each cell was selected and indexed. The evenness of fluorescence intensity (E) is defined as follows:

$$E = 1 - \frac{\sigma}{\mu}$$

where σ and μ stand for standard deviation and mean of intensities of every single pixel inside each cell. Fig. 5C shows the normalized mean fluorescence intensity and the evenness of fluorescence intensity of individual cell. The average evenness was 0.49, indicating

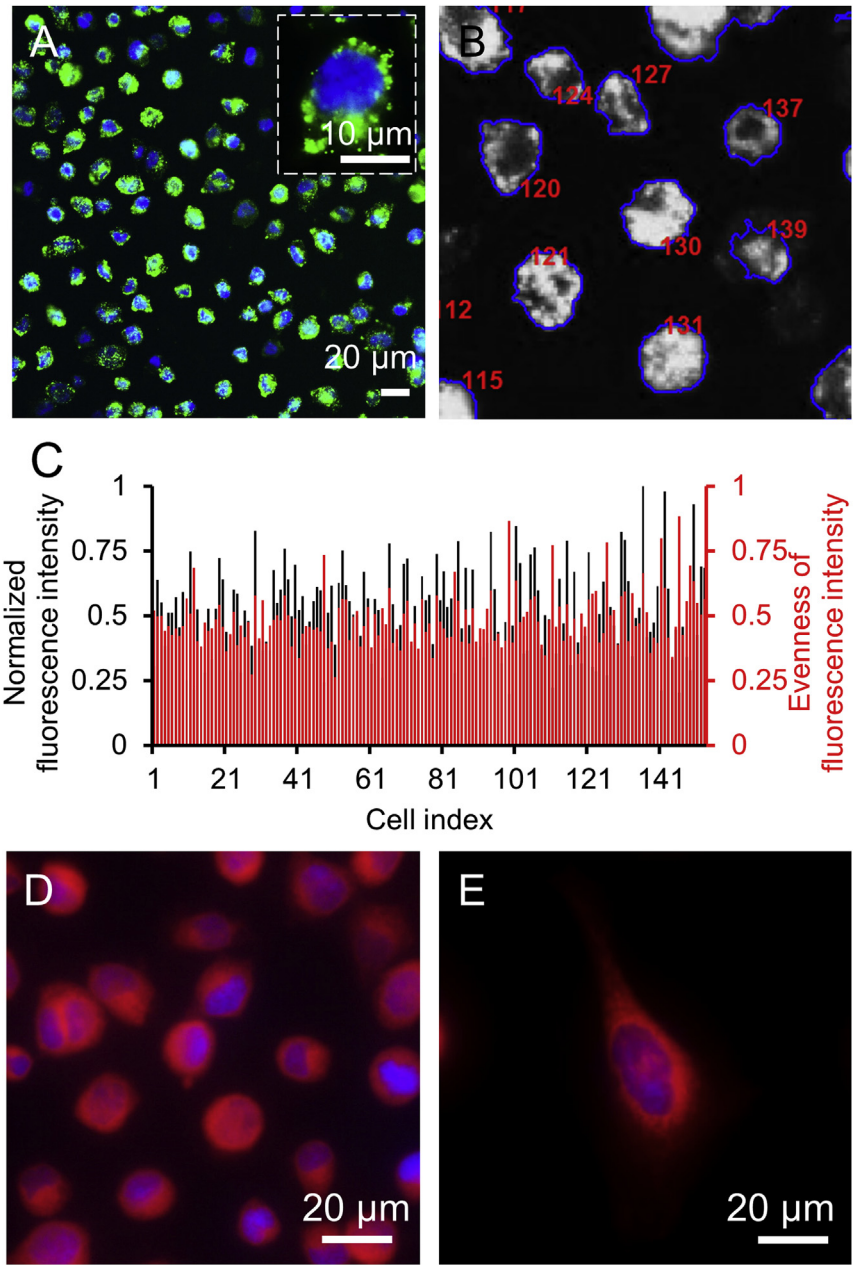

Fig. 5. Fluorescence image of an array of cells after detecting ROS (green) (A), where an enlarged image is shown as inset. Grayscale image (B) of MATLAB processed image, where individual cells were selected and indexed. ROS signal intensities of 153 individual cells (C), where black bars and red bars are fluorescence intensity and evenness of intensity, respectively. Fluorescence image of an array of cells after staining mitochondria (D), in comparison to a cell cultured on normal tissue culture plate (E). (For interpretation of the references to colour in this figure legend, the reader is referred to the web version of this article.)

that fluorescence intensities of majority of cells at sub-cellular level were highly non-uniform. In addition, each cell has a unique set of values for mean and evenness of intensity and cell-to-cell variation was large. For example, cell indexed with 120 has an intensity of 0.46, and cell indexed with 131 has an intensity of 0.59. The one indexed with 120 has a lower evenness of 0.42, while one indexed with 131 has a higher evenness of 0.79. The indexed array makes it possible to correlate a large amount of measurements to a large number of cells for further analysis such as evaluating oxidative damage to gene expression using FISH. In addition, this method is compatible with single-molecular FISH after sample clearing approach [42].

ROS are produced instantaneous by radiolysis of water, or secondarily by biological sources such as mitochondria in mammlian cells [43–45]. The sub-cellular distribution of ROS signal can be associated with distribution of mitochondria since it's not evenly distributed in the cells which otherwise would be caused by radiolysis of water. Mitochondria were stained as red in Fig. 5D, where individual mitochondrial structure is not clear in the arrayed cells. In comparison, the filament-like mitochondria can be seen in cells seeded onto a normal culture plate (Fig. 5E). This is because mitochondria in arrayed cells cannot be extended as much as those in non-arrayed cells that spread to a large area and separate from others. The resolution can be increased using advanced imaging techniques such as confocal or super-resolution microscope.

4. Conclusions

A single cell array based toxicity assay was established to provide sub-cellular toxicity information of a large population of cells. Cell array was formed by attaching cells to an array of positively charge polyelectrolytes. By physically placing cells at the same height and ordered locations, issues of overlapping and random distribution of cells were solved completely. The image processing softwares developed allowed rapid, unbiased and automate extraction of toxicity information without user interference. Cell toxicities upon exposure to ionizing X-ray radiation were simultaneously obtained at three distinct levels. Individual cells response heterogeneously at sub-cellular levels even if they were from the same population and from the same culture, and the results have also been statistically analyzed to differentiate cell populations based on their responses to radiation.

Acknowledgements

This project has been supported with a Director's New Innovator Award 1DP2EB016572 from National Institutes of Health.

References

[1] R.H. Shoemaker, The NCI60 human tumour cell line anticancer drug screen, Nat. Rev. Cancer 6 (2006) 813–823.
[2] C. Lam, J.T. James, R. McCluskey, S. Arepalli, R.L. Hunter, A review of carbon nanotube toxicity and assessment of potential occupational and environmental health risks, Crit. Rev. Toxicol. 36 (2008) 189–217.
[3] C.F. Jones, D.W. Grainger, In vitro assessments of nanomaterial toxicity, Adv. Drug Deliv. Rev. 61 (2009) 438–456.
[4] Q. Wang, Y. Bao, X. Zhang, P.R. Coxon, U.A. Jayasooriya, Y. Chao, Uptake and toxicity studies of poly-acrylic acid functionalized silicon nanoparticles in cultured mammalian cells, Adv. Healthc. Mater. 1 (2012) 189–198.
[5] J. Sikkema, J.A.M. Bont, B. Poolman, Mechanisms of membrane toxicity of hydrocarbons, Microbiol. Rev. 59 (1995) 201–222.
[6] P.V. AshaRani, G.L.K. Mun, M.P. Hande, S. Valiyaveettil, Cytotoxicity and genotoxicity of silver nanoparticles in human cells, ACS Nano 3 (2009) 279–290.
[7] D. Fischera, Y. Li, B. Ahlemeyerc, J. Krieglsteinc, T. Kissel, In vitro cytotoxicity testing of polycations: influence of polymer structure on cell viability and-hemolysis, Biomaterials 24 (2003) 1121–1131.
[8] M.S. Lawrence, P. Stojanov, P. Polak, G.V. Kryukov, K. Cibulskis, A. Sivachenko, S.L. Carter, C. Stewart, C.H. Mermel, S.A. Roberts, A. Kiezun, P.S. Hammerman, A. McKenna, Y. Drier, L. Zou, A.H. Ramos, T.J. Pugh, N. Stransky, E. Helman, J. Kim, C. Sougnez, L. Ambrogio, E. Nickerson, E. Shefler, M.L. Cortes, D. Auclair, G. Saksena, D. Voet, M. Noble, D. DiCara, P. Lin, L. Lichtenstein, D.I. Heiman, T. Fennell, M. Imielinski, B. Hernandez, E. Hodis, S. Baca, A.M. Dulak, J. Lohr, D.A. Landau, C.J. Wu, J. Melendez-Zajgla, A. Hidalgo-Miranda, A. Koren, S.A. McCarroll, J. Mora, R.S. Lee, B. Crompton, R. Onofrio, M. Parkin, W. Winckler, K. Ardlie, S.B. Gabriel, C.W. Roberts, J.A. Biegel, K. Stegmaier, A.J. Bass, L.A. Garraway, M. Meyerson, T.R. Golub, D.A. Gordenin, S. Sunyaev, E.S. Lander, G. Getz, Mutational heterogeneity in cancer and the search for new cancer-associated genes, Nature 499 (2013) 214–218.
[9] J.M. Raser, E.K. O'Shea, Noise in gene expression: origins, consequences, and control, Science 309 (2005) 2010–2013.
[10] R.R. Tice, E. Agurell, D. Anderson, B. Burlinson, A. Hartmann, H. Kobayashi, Y. Miyamae, E. Rojas, J.-C. Ryu, Y.F. Sasaki, Single cell gel/comet assay: guidelines for in vitro and in vivo genetic toxicology testing, Environ. Mol. Mutagen. 35 (2000) 206–221.
[11] D.D.W. Cornelison, B.J. Wold, Single-cell analysis of regulatory gene expression in quiescent and activated mouse skeletal muscle satellite cells, Dev. Biol. 191 (1997) 270–283.
[12] D. Ryan, K. Ren, H. Wu, Single-cell assays, Biomicrofluidics 5 (2011) 21501.
[13] E. Brouzes, M. Medkova, N. Savenelli, D. Marran, M. Twardowski, J.B. Hutchison, J.M. Rothberg, D.R. Link, N. Perrimon, M.L. Samuels, Droplet microfluidic technology for single-cell high-throughput screening, Proc. Natl. Acad. Sci. U. S. A. 106 (2009) 14195–14200.
[14] J. Clausell-Tormos, D. Lieber, J.C. Baret, A. El-Harrak, O.J. Miller, L. Frenz, J. Blouwolff, K.J. Humphry, S. Koster, H. Duan, C. Holtze, D.A. Weitz, A.D. Griffiths, C.A. Merten, Droplet-based microfluidic platforms for the encapsulation and screening of Mammalian cells and multicellular organisms, Chem. Biol. 15 (2008) 427–437.
[15] A.R. Wheeler, W.R. Throndset, R.J. Whelan, A.M. Leach, R.N. Zare, Y.H. Liao, K. Farrell, I.D. Manger, A. Daridon, Microfluidic device for single-cell analysis, Anal. Chem. 75 (2003) 3581–3586.
[16] M. He, J.S. Edgar, G.D.M. Jeffries, R.M. Lorenz, J.P. Shelby, D.T. Chiu, Selective encapsulation of single cells and subcellular organelles into picoliter- and femtoliter-volume droplets, Anal. Chem. 77 (2005) 1539–1544.
[17] J. Chung, H. Shao, T. Reiner, D. Issadore, R. Weissleder, H. Lee, Microfluidic cell sorter (muFCS) for on-chip capture and analysis of single cells, Adv. Healthc. Mater. 1 (2012) 432–436.
[18] L.C. Wienkers, T.G. Heath, Predicting in vivo drug interactions from in vitro drug discovery data, Nat. Rev. Drug Discov. 4 (2005) 825–833.
[19] T. Iwatmbo, N. Hirota, T. Ooie, H. Suzuki, N. Shimada, K. Chiba, T. Ishizaki, C.E. Green, C.A. Tyson, Y. Sugiyama, Prediction of in vivo drug metabolism in the human liver from in vitro metabolism data, Pharmacol. Ther. 73 (1997) 147–171.
[20] R.J. R, A. Folch, Large-scale single-cell trapping and imaging using microwell arrays, Anal. Chem. 77 (2005) 5628–5634.
[21] M. Ochsner, M.R. Dusseiller, H.M. Grandin, S. Luna-Morris, M. Textor, V. Vogel, M.L. Smith, Micro-well arrays for 3D shape control and high resolution analysis of single cells, Lab a chip 7 (2007) 1074–1077.
[22] I. Biran, D.R. Walt, Optical imaging fiber-based single live cell arrays: a high-density cell assay platform, Anal. Chem. 74 (2002) 3046–3054.
[23] B. Dykstra, J. Ramunas, D. Kent, L. McCaffrey, E. Szumsky, L. Kelly, K. Farn, A. Blaylock, C. Eaves, E. Jervis, High-resolution video monitoring of hematopoietic stem cells cultured in single-cell arrays identifies new features of self-renewal, Proc. Natl. Acad. Sci. U. S. A. 103 (2006) 8185–8190.
[24] G.T. Salazar, Y. Wang, G. Young, M. Bachman, C.E. Sims, G.P. Li, A.N. L, Micropallet arrays for the separation of single, adherent cells, Anal. Chem. 79 (2007) 682–687.
[25] W.C. Lee, S. Rigante, A.P. Pisano, F.A. Kuypers, Large-scale arrays of picolitre chambers for single-cell analysis of large cell populations, Lab a chip 10 (2010) 2952–2958.
[26] Y. Liu, B. Kirkland, J. Shirley, Z. Wang, P. Zhang, J. Stembridge, W. Wong, S. Takebayashi, D.M. Gilbert, S. Lenhert, J. Guan, Development of a single-cell array for large-scale DNA fluorescence in situ hybridization, Lab a chip 13 (2013) 1316–1324.
[27] Y. Qiao, J. An, L. Ma, Single cell array based assay for in vitro genotoxicity study of nanomaterials, Anal. Chem. 85 (2013) 4107–4112.
[28] T.M. Gierahn, M.H. Wadsworth 2nd, T.K. Hughes, B.D. Bryson, A. Butler, R. Satija, S. Fortune, J.C. Love, A.K. Shalek, Seq-Well: portable, low-cost RNA sequencing of single cells at high throughput, Nat. methods 14 (2017) 395–398.
[29] Y. Qiao, C. Wang, M. Su, L. Ma, Single cell DNA damage/repair assay using HaloChip, Anal. Chem. 84 (2012) 1112–1116.
[30] C.P. Tan, B.R. Seo, D.J. Brooks, E.M. Chandler, H.G. Craighead, C. Fischbach, Parylene peel-off arrays to probe the role of cell-cell interactions in tumour angiogenesis, Integr. Biol. 1 (2009) 587–594.
[31] A. Azioune, M. Storch, M. Bornens, M. Théry, M. Piel, Simple and rapid process for single cell micro-patterning, Lab a chip 9 (2009) 1640–1642.
[32] S. Yamahira, S. Yamaguchi, M. Kawahara, T. Nagamune, Collagen surfaces modified with photo-cleavable polyethylene glycol-lipid support versatile single-cell arrays of both non-adherent and adherent cells, Macromol. Biosci. 14 (2014) 1670–1676.
[33] E.I. Finkelstein, P.H. Chao, C.T. Hung, J.C. Bulinski, Electric field-induced polarization of charged cell surface proteins does not determine the direction of galvanotaxis, Cell Motil. cytoskel. 64 (2007) 833–846.

[34] K. Kato, K. Umezawa, D.P. Funeriu, M. Miyake, J. Miyake, T. Nagamune, Immobilized culture of nonadherent cells on an oleyl poly(ethylene glycol) ether-modified surface, Biotechniques 35 (2003) 1014–1018.
[35] A.C. Anselmo, J.B. Gilbert, S. Kumar, V. Gupta, R.E. Cohen, M.F. Rubner, S. Mitragotri, Monocyte-mediated delivery of polymeric backpacks to inflamed tissues: a generalized strategy to deliver drugs to treat inflammation, Journal of controlled release, official J. Control. Release Soc. 199 (2015) 29–36.
[36] Z. Wang, P. Zhang, B. Kirkland, Y. Liu, J. Guan, Microcontact printing of polyelectrolytes on PEG using an unmodified PDMS stamp for micropatterning nanoparticles, DNA, proteins and cells, Soft Matter 8 (2012) 7630–7637.
[37] S. Kuwamoto, S. Akiyama, T. Fujisawa, Radiation damage to a protein solution, detected by synchrotron X-ray small-angle scattering: dose-related considerations and suppression by cryoprotectants, J. Synchrotron Radiat. 11 (2004) 462–468.
[38] K.S. Ambe, U.S. Kumta, A.L. Tappel, Radiation damage to cytochrome c and hemoglobin, Radiat. Res. 15 (1961) 709–719.
[39] Z. Somosy, Radiation response of cell organelles, Micron 31 (2000) 165–181.
[40] R. Veselská, R. Janisch, The effect of UV irradiation on changes in cytoskeleton and viability of mouse fibroblast L929 cell line, Scr. Med. 73 (2000) 393–408.
[41] E.I. Azzam, J.P. Jay-Gerin, D. Pain, Ionizing radiation-induced metabolic oxidative stress and prolonged cell injury, Cancer Lett. 327 (2012) 48–60.
[42] J.R. Moffitta, J. Hao, D.B. Mukkua, T. Lu, C. Dulac, X. Zhuang, High-performance multiplexed fluorescence in situ hybridization in culture and tissue with matrix imprinting and clearing, Proc. Natl. Acad. Sci. U. S. A. 113 (2017) 14456–14461.
[43] M.P. Murphy, How mitochondria produce reactive oxygen species, Biochem. J. 417 (2009) 1–13.
[44] T. Yamamori, H. Yasui, M. Yamazumi, Y. Wada, Y. Nakamura, H. Nakamura, O. Inanami, Ionizing radiation induces mitochondrial reactive oxygen species production accompanied by upregulation of mitochondrial electron transport chain function and mitochondrial content under control of the cell cycle checkpoint, Free Radic. Biol. Med. 53 (2012) 260–270.
[45] G. Feng, W. Qin, Q. Hu, B.Z. Tang, B. Liu, Cellular and mitochondrial dual-targeted organic dots with aggregation-induced emission characteristics for image-guided photodynamic therapy, Adv. Healthc. Mater. 4 (2015) 2667–2676.